

Self-Recoverable Symmetric Protonic Ceramic Fuel Cell with Smart Reversible Exsolution/Dissolution Electrode

Yuhao Wang, Zheng Wang, Kaichuang Yang, Jiapeng Liu, Yufei Song, Jingwei Li, Zhiwei Hu, Matthew J. Robson, Zhiqi Zhang, Yunfeng Tian, Shenjun Xu, Ying Lu, Ho Mei Law, Feng Liu, Qing Chen, Zhibin Yang,* and Francesco Ciucci*

This study unveils a novel concept of symmetric protonic ceramic fuel cells (symm-PCFCs) with the introduction of a self-recoverable electrode design, employing the innovative material $\text{BaCo}_{0.4}\text{Fe}_{0.4}\text{Zr}_{0.1}\text{Y}_{0.1}\text{O}_{3-\delta}$ (BCFZY). This research marks a significant milestone as it demonstrates the bi-functional electrocatalytic activity of BCFZY for the first time. Utilizing density functional theory simulations, the molecular orbital interactions and defect chemistry of BCFZY are explored, uncovering its unique capability for the reversible exsolution and dissolution of Co-Fe nanoparticles under redox conditions. This feature is pivotal in promoting both hydrogen oxidation and oxygen reduction reactions. Leveraging this insight, a cell is fabricated exhibiting high electrocatalytic activity and fuel flexibility as evidenced by the peak power densities of ≈ 350 , 287, and 221 mW cm^{-2} (at 600 °C) with hydrogen, methanol, and methane as fuels, respectively. Experiments also show that the reversible exsolution/dissolution mitigates performance degradation, enabling prolonged operational life through self-recovery. This approach paves the way for novel, advanced, durable, and commercially viable symm-PCFCs.

1. Introduction

Owing to their high efficiency and fuel flexibility, high-temperature ceramic fuel cells are among the most promising, next-generation clean energy storage and conversion technologies.^[1] Among the various configurations,^[2] symmetric ceramic fuel cells have attracted considerable research attention, since using identical cathode and anode materials can lead to significant cost reductions.^[3] Despite their promise, symmetric fuel cells are still far from commercialization due to their limited performance.^[4] These cells are typically supported by a thick electrolyte. Therefore, if conventional oxygen conductors, such as yttria-stabilized zirconia, are used, the operation must occur at high temperatures (typically between 700 and 1000 °C) to accelerate oxygen transport.^[5] However,

Y. Wang, J. Liu, Y. Song, M. J. Robson, Y. Tian, Q. Chen, F. Ciucci
Department of Mechanical and Aerospace Engineering
The Hong Kong University of Science and Technology
Clear Water Bay, Hong Kong 999077, P. R. China
E-mail: francesco.ciucci@ust.hk, francesco.ciucci@uni-bayreuth.de

Z. Wang
Institute for Advanced Study
Shenzhen University
Shenzhen 518060, P. R. China

K. Yang, Z. Yang
Research Center of Solid Oxide Fuel Cell
China University of Mining and Technology-Beijing
Beijing 100083, P. R. China
E-mail: yangzhibin@cumtb.edu.cn

K. Yang, Y. Lu
School of Engineering
Westlake University
Hangzhou 310024, P. R. China

J. Liu
School of Advanced Energy
Sun Yat-Sen University
Shenzhen 518107, P. R. China

J. Li, S. Xu, H. M. Law, F. Ciucci
Chair of Electrode Design for Electrochemical Energy Systems
University of Bayreuth
Weierstrasse 26, 95448 Bayreuth, Bavaria, Germany

J. Li, S. Xu, H. M. Law, F. Ciucci
Bavarian Center for Battery Technology (BayBatt)
University of Bayreuth
Universitätsstraße 30, 95447 Bayreuth, Germany

Z. Hu
Max-Planck-Institute for Chemical Physics of Solids
Nöthnitzer Str. 40, 01187 Dresden, Germany

Z. Zhang
Key Laboratory of Energy Thermal Conversion and Control of Ministry of Education
School of Energy and Environment
Southeast University
Nanjing 210096, P. R. China

Y. Tian
Jiangsu Key Laboratory of Coal-based Greenhouse Gas Control and Utilization
School of Materials Science and Physics
China University of Mining and Technology
Xuzhou 221116, P. R. China

The ORCID identification number(s) for the author(s) of this article can be found under <https://doi.org/10.1002/adfm.202404846>

© 2024 The Author(s). Advanced Functional Materials published by Wiley-VCH GmbH. This is an open access article under the terms of the [Creative Commons Attribution-NonCommercial](https://creativecommons.org/licenses/by-nc/4.0/) License, which permits use, distribution and reproduction in any medium, provided the original work is properly cited and is not used for commercial purposes.

DOI: 10.1002/adfm.202404846

operating at high temperatures increases system complexity, accelerates component degradation, and requires the use of costly sealing and interconnect materials. Using proton-conducting ceramic electrolytes, which leverage the higher mobility and lower transport barrier of protons (relative to oxygen ions), can overcome these issues. For instance, it has been shown that symmetric protonic ceramic fuel cells (symm-PCFCs) can be operated between 500 and 600 °C.^[6] Nevertheless, the effectiveness of symm-PCFCs is constrained by the requirement for electrodes to be bi-functionally active in both hydrogen oxidation reaction (HOR) and oxygen reduction reaction (ORR).^[3,7] Therefore, developing catalytically active perovskite-based electrodes for symm-PCFCs has become a pressing need.

Incorporating Fe⁰ and Co⁰ nanoparticles (NPs) into perovskite scaffolds significantly enhances HOR activity.^[8] Conventional infiltration methods, which impregnate nitrate precursors into perovskites, followed by firing and reduction,^[9] often lead to weak perovskite-NP interaction and NP agglomeration at high temperatures.^[10] Our research counters this by employing an exsolution-like approach, promoting uniform NP distribution on the perovskite scaffold.^[11] This method involves breaking perovskite transition metal-oxygen (TM–O) bonds under hydrogen reduction.^[12] However, the disruption of these bonds and the ensuing exsolution actually leads to the decomposition and structural degradation of the perovskite.^[13] To remedy this decomposition, the structure is subsequently reconstructed, and NPs are redissolved through re-oxidation.^[14] Besides exhibiting HOR activity, a bi-functional perovskite electrode must also demonstrate ORR activity. The presence of weak TM–O bonds is advantageous, as it facilitates oxygen release thus enhancing ORR performance. This enhancement is attributed to the increase in the production of oxygen vacancies and hydroxide ions,^[15] both of which are crucial for efficient ORR electrocatalysis.^[16]

Ideally, electrode materials for symm-PCFCs must balance TM–O bond strength, which should be sufficiently strong to ensure lattice stability, yet weak enough to allow for the exsolution of HOR-active NPs and the generation of oxygen vacancies. These characteristics are generally unachievable with perovskites containing only one type of transition metal. Typically, non-variable valence elements, like Zr and Y, tend to form strong TM–O bonds, whereas transition metals with variable valence states, such as Co and Fe, are known to create weaker TM–O bonds.^[17] Consequently, strategically combining fixed and variable-valence transition metals within the perovskite structure may result in an “optimal” mix of TM–O bond strengths. Such a combination can effectively harness the benefits of both weak and strong bonding toward electro-catalytic activity and stability, thereby enhancing the overall performance and stability of symm-PCFC electrodes.

In this study, we selected BaCo_{0.4}Fe_{0.4}Zr_{0.1}Y_{0.1}O_{3-δ} (BCFZY), which contains four distinct transition metals (Co, Fe, Y, and Zr)

in its B-site, as the model material, and uncovered its untapped potential.^[18] Unlike previous studies where BCFZY was used solely as an oxygen electrocatalyst,^[19] this work represents the first exploration of BCFZY as a hydrogen/oxygen bi-functional electrocatalyst. We employ a combination of molecular orbital theory analysis and density functional theory (DFT) calculations, providing a comprehensive analysis of TM–O bonds within BCFZY and their profound influence on oxygen vacancy formation, hydration, and NP exsolution. Under cathodic conditions, the weak Co–O and Fe–O bonds effectively lower the energy barrier for oxygen release, thus promoting the generation of oxygen vacancies and protons. Conversely, in anodic conditions, these same weakened TM–O bonds facilitate the segregation of transition metal atoms onto the perovskite surface, leading to NP formation and enhanced electrocatalytic activity.^[20] In contrast, the robust Y–O and Zr–O bonds within BCFZY exhibit greater resistance to breakage, contributing significantly to the overall structural stability of the material. Moreover, the low energy barrier for Co and Fe segregation supports their migration from the surface to the bulk under oxidizing conditions. As bonding is less energetic, the re-formation of Co–O and Fe–O bonds becomes more readily achievable.^[21]

To validate these insights, we fabricated a symm-PCFC in which BCFZY was employed for the first time as a bi-functional electrode, with BaZr_{0.1}Ce_{0.7}Y_{0.1}Yb_{0.1}O_{3-δ} (BZCYYb) serving as the electrolyte. Electrochemical impedance spectroscopy revealed an enhancement in the electrocatalytic activity of BCFZY following its reduction and subsequent exsolution of NPs. Specifically, the area-specific resistance (ASR) was halved (0.71 Ω cm⁻² at 600 °C in hydrogen atmosphere) compared to its value before reduction (1.42 Ω cm⁻²). Furthermore, the symm-PCFC achieved peak power densities of ≈350, 233, and 131 mW cm⁻² at 600, 550, and 500 °C, respectively, with hydrogen as the fuel. The symm-PCFC also recovered from prolonged exposure to reducing conditions through a simple cathode-anode atmospheric swap achieved by switching the gas feed lines. Interestingly, the cell sustained multiple repeated cathode-anode atmospheric swaps without detectable performance loss. Additionally, the symm-PCFC showed resistance to carbon coking when operating in methanol or methane, highlighting its versatility in fuel flexibility. This electrode design strategy not only enhances the performance and durability of symm-PCFCs but also opens a wide and promising avenue for extending their lifespan and propelling their commercialization.

2. Results and Discussion

2.1. DFT Calculations

Oxygen vacancies and hydroxide defects strongly influence charge transport and electrode reaction kinetics in PCFC cathodes. Therefore, we computed^[22] the lowest values of oxygen vacancy formation energy ($E_{V_{O}}$), and hydration energy (E_{hydr}) for BCFZY (a well-established excellent air electrode material^[19]) considering all possible defect-containing sites (Figure 1a; Figure S1 and Table S1, Supporting Information). BCFZY exhibited remarkably low $E_{V_{O}}$ of 0.10 eV (consistent with a previous report^[23]), which is significantly lower than other

F. Liu
Yunnan Precious Metals Lab Co., LTD
Kunming 650100, P. R. China
Z. Yang
Beijing Huairou Laboratory
Beijing 101400, China

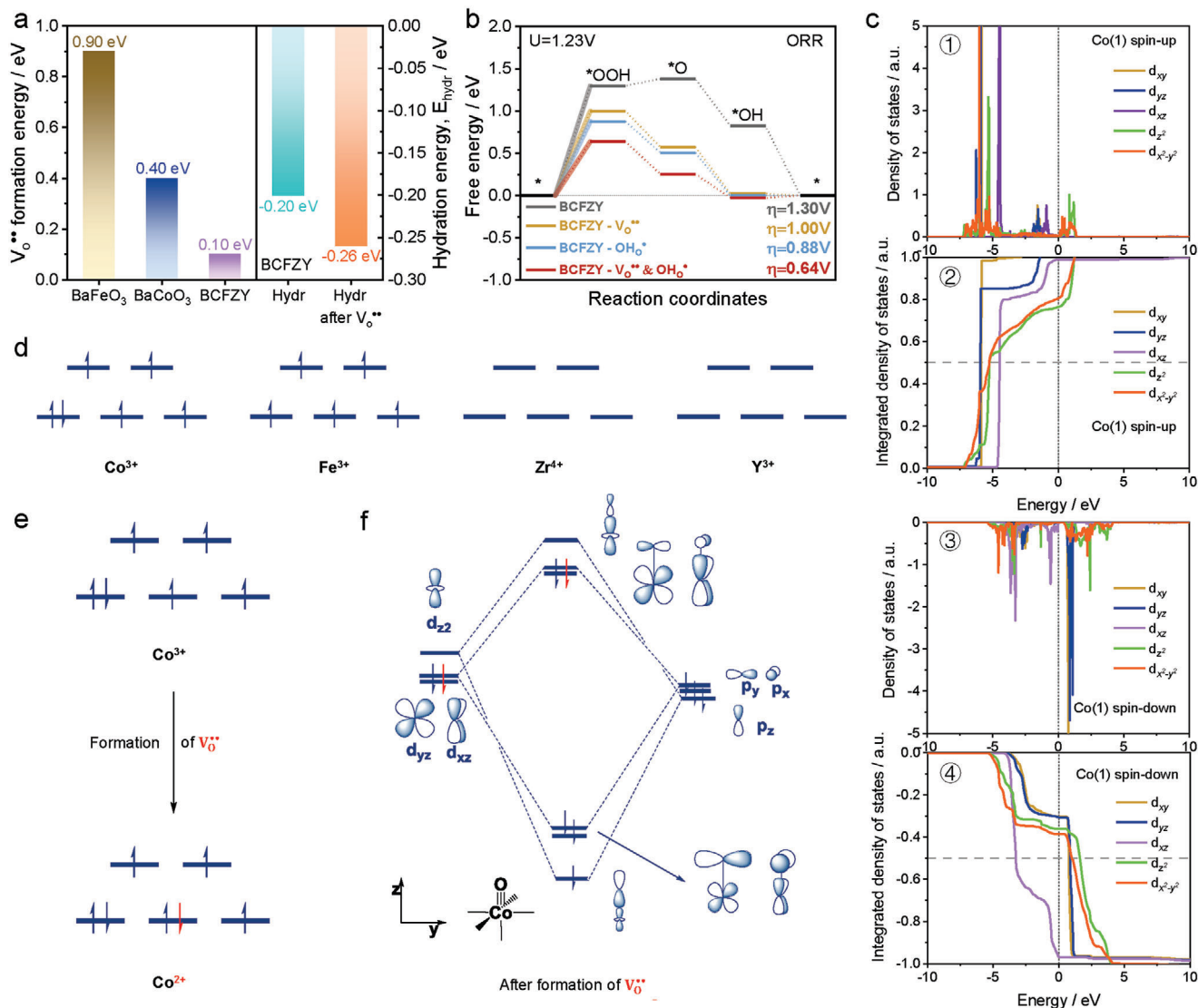


Figure 1. DFT calculations and molecular orbital analysis of BCFZY. a) Calculated V_o^{**} formation energy, $E_{V_o^{**}}$, for $BaFeO_3$, $BaCoO_3$, and BCFZY and hydration energy, E_{hydr} , for BCFZY and BCFZY with one oxygen vacancy. b) ORR free energies computed at the BCFZY(001) surface with an oxygen vacancy, V_o^{**} , and a hydroxide ion, OH_o^{*} . c) PDOS and IPDOS of Co(1) in spin-up and spin-down channels, respectively. d) The ligand field of the transition metal atoms (Co, Fe, Zr, and Y) in BCFZY. e) The ligand field of Co before and after the formation of a V_o^{**} . f) The Co–O bond orbital interaction.

state-of-the-art perovskites, such as cubic $BaFeO_3$ (0.79 eV for calculation and 0.90 eV for literature^[24]), $BaCoO_3$ (0.51 eV for calculation and 0.40 eV for literature^[25]), and $Ba_{0.5}Sr_{0.5}Co_{1-y}Fe_yO_{3-\delta}$ (BSCF, 1.34–1.40 eV).^[26] Interestingly, pristine BCFZY had an E_{hydr} of -0.20 eV, decreasing to -0.26 eV upon the introduction of an oxygen vacancy at the lowest $E_{V_o^{**}}$ position. The lowered hydration energy of BCFZY when introducing oxygen vacancies is consistent with the literature^[27] and was also confirmed experimentally (Figures S2–S5, Supporting Information).

To compute the ORR overpotential (η) for both pristine and defect-containing BCFZY, we computed ORR free energy diagrams^[28] with details provided in Supporting Information Section 1.5. The simulations were carried out using a BCFZY (001) slab, consistent with transmission electron microscope (TEM) characterization (Figure S6, Supporting Information). The

following four slab models were considered: 1) pristine slab; 2) slab with a single V_o^{**} ; 3) slab with a single OH_o^{*} ; 4) slab with $V_o^{**} + OH_o^{*}$ pair. In comparison to the bare surface, the presence of either V_o^{**} or OH_o^{*} reduces the ORR overpotential, notably decreasing it from $\eta = 1.30$ V on the bare surface to $\eta = 1.00$ V (in the presence of V_o^{**}) and $\eta = 0.88$ V (in the presence of OH_o^{*}), respectively. The η dropped further to 0.64 V when both V_o^{**} and OH_o^{*} were present. As V_o^{**} and OH_o^{*} are electron donors, they reduced the surface of BCFZY, effectively elevating its Fermi level. In turn, BCFZY donated electrons more easily to O_2 , facilitating not only O_2 adsorption but also the subsequent formation of OOH^* through the rate-limiting reaction $* \rightarrow OOH^*$ ^[29] (Figure 2b).

To elucidate the TM–O orbital interactions in BCFZY, we made detailed evaluations of energy levels, electron occupations, and orbital overlaps of Co, Fe, Y, and Zr. This involved analyzing

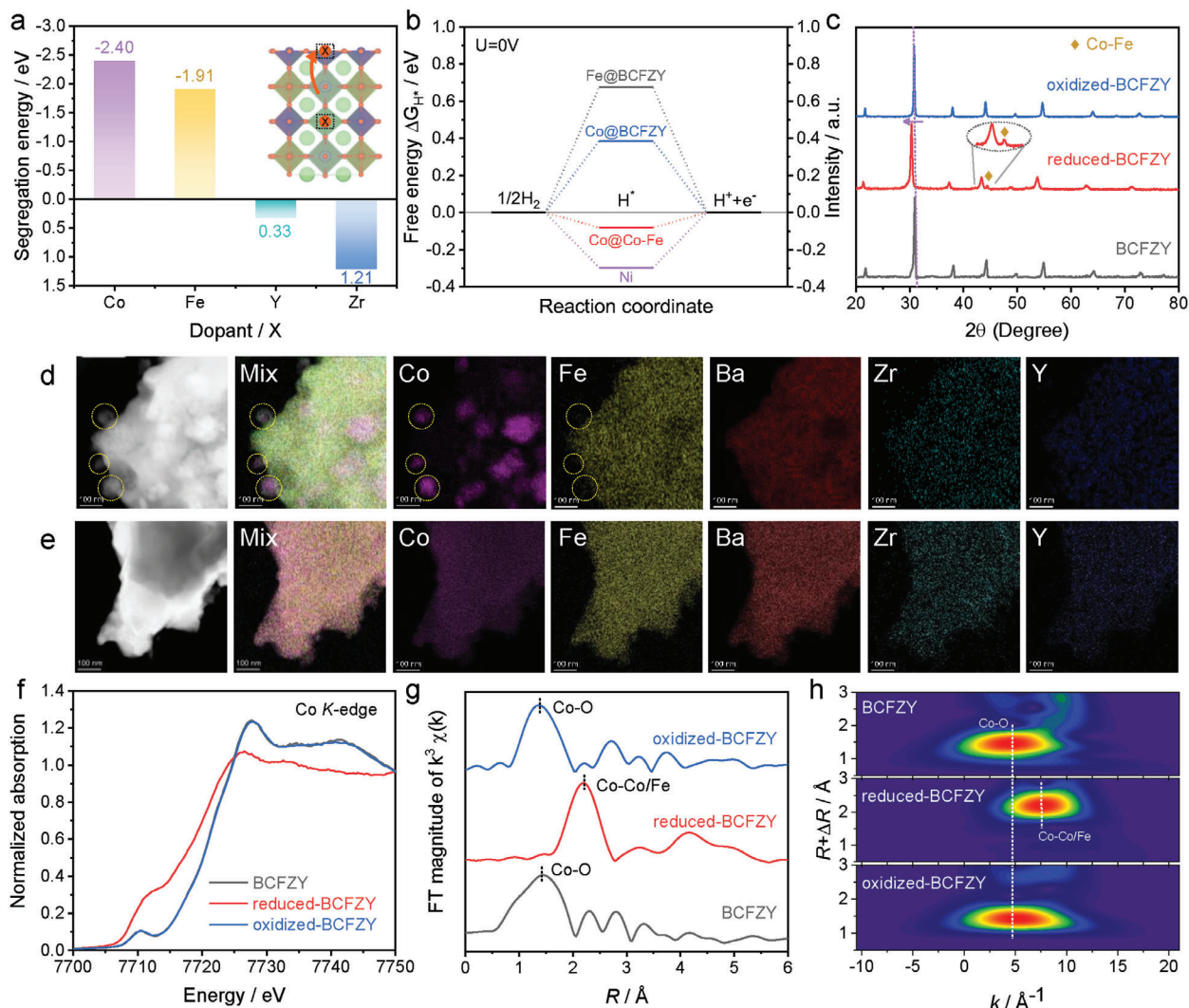


Figure 2. Crystal structure and compositional analysis of BCFZY. a) Comparison of the exsolution energies with the dopant ($X = \text{Co}, \text{Fe}, \text{Zr}, \text{and Y}$) materials. The inset schematic illustration of the model used for the calculations of exsolution energy. b) The calculated free energy diagram for hydrogen evolution of the BCFZY (001), Ni(111), and exsolved Co-Fe(001) surface. c) XRD patterns of as-synthesized BCFZY, reduced-BCFZY, and oxidized-BCFZY. STEM image and EDS mapping of d) reduced-BCFZY, and e) oxidized-BCFZY powders. f) Normalized XANES spectra at the Co K edge. g) k^3 -weighted R-space Fourier transformed spectra from EXAFS. h) Wavelet transforms for the k^3 -weighted EXAFS signals of BCFZY, reduced-BCFZY, and oxidized-BCFZY.

their projected density of states (PDOS) and integrated projected density of states (IPDOS).^[30] In our computational model, we individually analyzed three distinct positions of Co or Fe atoms, denoted as Co(1), Co(2), Co(3), Fe(1), Fe(2), and Fe(3), as illustrated in Figure S1 (Supporting Information). Specifically, for Co(1) and Co(3), all six Co–O bonds are exclusively connected to Co or Fe atoms; in the case of Fe(1) and Fe(3), four out of their six Fe–O bonds are linked to Zr or Y; meanwhile, for Fe(2) and Co(2), two out of the six Co/Fe–O bonds are connected to Zr or Y. As shown in Figure 1c, all d orbitals of Co(1) in the spin-up channel display their primary PDOS peaks below the Fermi energy (0 eV), indicating complete occupation of these orbitals. The IPDOS (Figure 1c) further supports this observation, showing that the occupancy rate of all d orbitals of Co(1) at the Fermi, that is, the integrated electronic state density at the Fermi energy, sig-

nificantly exceeds 0.5, signifying their full occupancy. Conversely, in the spin-down channel, the PDOS for four d orbitals of Co(1) is positioned above the Fermi energy, with IPDOS occupancy rates well below 0.5, signifying these orbitals are unoccupied. Notably, the d_{xz} orbital presents a major peak below the Fermi level with an occupancy rate near -1.0 , as indicated in Figure 1c. This suggests the existence of one d electron in the spin-down channel. Consequently, with five d electrons in the spin-up channel and one d electron in the spin-down channel, we can infer that Co(1) possesses a +3 oxidation state. Comparative analysis of Co(2) and Co(3) PDOS and IPDOS, as shown in Figures S7 and S8 (Supporting Information), leads to similar conclusions, thereby characterizing all Co cations as Co^{3+} .

Figures S9–S11 (Supporting Information) provide similar insight into the d orbitals of Fe(1), Fe(2), and Fe(3), respectively.

In all cases, the d orbitals of the Fe ions exhibit complete occupancy in the spin-up channel and are empty in the spin-down channel, implying that Fe(1), Fe(2), and Fe(3) correspond to high-spin-state Fe^{3+} . For Y and Zr (see Figures S12 and S13, Supporting Information, respectively), the primary peaks of the d orbitals are significantly higher than the Fermi energy. Additionally, the IPDOS occupancy rate at the Fermi level is close to 0, indicating the absence of d electrons in both the spin-up and spin-down channels. Thus, the oxidation states of Zr and Y can be identified as Zr^{4+} and Y^{3+} , respectively.

2.2. Molecular Orbital Analysis

The TM–O bond strength is influenced by the interaction of the TM and O orbitals.^[22] For instance, fully occupied bonding orbitals enhance bond strength, while the presence of electrons in the anti-bonding orbital tends to weaken bonds. To elucidate the impact of TM and O orbital interactions on bond strength in BCFZY, we analyzed the hybridization and bonding conditions between TM and O by considering the d orbitals of TM in both spin-up and spin-down channels. The scenario for Co^{3+} and Fe^{3+} in the spin-up channel is quite similar, with all d orbitals being fully occupied, leading to a pronounced repulsive interaction with the oxygen's p electrons. In contrast, the situation in the spin-down channel for Co^{3+} and Fe^{3+} is markedly different. For Co^{3+} , despite having four unoccupied d orbitals, the presence of a single d electron still results in a strong repulse of oxygen's p electrons. However, the spin-down channel of Fe^{3+} shows a completely unoccupied d -orbital configuration, thus facilitating strong hybridization with oxygen's p electrons.^[22] These differences in electron configuration suggest that the Co–O bond is weaker than the Fe–O bond.

We also explored how the d orbitals of Y^{3+} and Zr^{4+} and oxygen's p electrons interact with each other (Figure S14, Supporting Information). The d orbitals of Y^{3+} have higher energy than those of Zr^{4+} due to lower charges. Consequently, the energy difference between the d orbitals of Y^{3+} and the p orbitals of O^{2-} is larger than that between Zr^{4+} and O^{2-} , and hybridization between Y^{3+} and O^{2-} is weaker than that between Zr^{4+} and O^{2-} . This results in a relatively weaker Y–O bond than the Zr–O bond.^[6c,31] As shown in Figures S12–S14 (Supporting Information), the lower IPDOS value for Y relative to Zr also suggests that the Y–O bond is weaker than the Zr–O bond. Consequently, the TM–O bond strengths are ordered as follows $\text{Zr–O} > \text{Y–O} > \text{Fe–O} > \text{Co–O}$. As the Co–O bond is the weakest, the formation of $\text{V}_\text{O}^\bullet$ and $\text{OH}_\text{O}^\bullet$ occurs more easily near Co. This observation aligns with the outcomes of the defect chemical DFT calculations shown in Figure 1a and Figure S1 (Supporting Information), which indicate that the sites with the lowest formation energy for $\text{V}_\text{O}^\bullet$ and $\text{OH}_\text{O}^\bullet$ are the ones near Co–O. The generation of oxygen vacancies, which are electron donors,^[32] facilitates the reduction of Co^{3+} to Co^{2+} (Figure 1e). This process is energetically more favorable than the Fe^{3+} to Fe^{2+} reduction (Figures S7–S11, Supporting Information).

From the above analysis, it is evident that the Co–O bond is the weakest, with $\text{V}_\text{O}^\bullet$ and $\text{OH}_\text{O}^\bullet$ more likely to form near Co. Therefore, we analyzed the impact of $\text{V}_\text{O}^\bullet$ formation on the Co–O bond from a molecular orbital perspective (Figure 1f). The formation

of $\text{V}_\text{O}^\bullet$ introduces the additional electrons to the material, which initially serve to compensate for the existing ligand holes. As the ligand holes diminish, these electrons subsequently contribute to the reduction of Co. When Co ions undergo reduction, the electrons occupy the anti-bonding orbitals of the Co–O bond, consequently weakening these bonds. This weakening is conducive to the further reduction of Co ions.^[33] Both the attenuation of the Co–O bond and the reduction of Co facilitate the generation of n -type donors, such as $\text{V}_\text{O}^\bullet$ and $\text{OH}_\text{O}^\bullet$.^[6c] In summary, the presence of $\text{V}_\text{O}^\bullet$ and $\text{OH}_\text{O}^\bullet$ further diminishes the strength of the Co–O bond, which in turn reduces Co and concomitantly decreases the energy necessary to create $\text{V}_\text{O}^\bullet$ and $\text{OH}_\text{O}^\bullet$.

2.3. Exsolution Mechanism

To evaluate the tendency of BCFZY's transition metals to exsolve, the segregation energies of Co, Fe, Y, and Zr were calculated. Our selection of the most stable terminal surface on the BCFZY(001) plane aligns with TEM data (Figure S6, Supporting Information) and literature reports.^[34] The Co, Fe, Y, and Zr segregation energies were -2.40 , -1.91 , 0.33 , and 1.21 eV (Figure 2a), respectively, implying that Co and Fe may migrate more easily to the surface than Y and Zr due to the weaker Co–O and Fe–O bonds. Figures S15 and S16 (Supporting Information) report the PDOS and IPDOS for both surface and bulk Co and Fe, revealing that the IPDOS occupancy for the d_{z^2} orbital of surface Co and Fe are substantially higher at the Fermi level compared to the bulk. While Fe exhibits similar behavior to Co, the IPDOS indicates that the number of occupied electrons in Fe is lower than in Co (Figures S17 and S18, Supporting Information), implying that Fe is slightly less reducible and exsolvable than Co in agreement with the higher computed segregation energy of Fe relative to Co (Figure 2a).

To evaluate the HOR activity of exsolved NPs^[11,20a,35] and bulk perovskite materials, we used the H^* adsorption energy as an indicator.^[2d,36] We computed adsorption energy calculations across all potential adsorption sites, including various top and bridge sites. For the BCFZY(001), we considered the impact of different terminations. For the Co–Fe(001) surface, consistent with literature findings,^[37] we identified the configuration with the lowest energy as the most likely pathway for HOR. The simulations (Figure 2b) reveal that the Co top site on the Co–Fe(001) surface is the most favorable position for H^* adsorption, corresponding to adsorption-free energy as low as -0.08 eV. This value is not only better than that of the Co and Fe top sites on the BCFZY(001) surface, which are 0.39 and 0.67 eV, respectively but also superior to the -0.30 eV on the Ni(111) surface. These simulations indicate that Co–Fe NPs improve H^* adsorption and thus facilitate HOR activity.

2.4. Reversible Exsolution/Dissolution

We carried out a 24-h ASR test on a symmetric cell to determine how exsolved NPs first enhance electrocatalysis and then degrade it (Figure S19, Supporting Information). Employing pure hydrogen as the feed gas, electrochemical impedance spectroscopy (EIS) data were collected every 30 min at a temperature of 600°C .

The initial ASR value of $1.42 \Omega \text{ cm}^{-2}$ significantly decreased to $\approx 0.71 \Omega \text{ cm}^{-2}$ within the first 6 h, indicative of enhanced HOR activity due to NP exsolution. However, a marginal rise to $0.77 \Omega \text{ cm}^{-2}$ at the 24th h suggested the agglomeration of the exsolved NPs.^[38] To assess the correlation between the exsolution phenomenon of BCFZY and temperature, we subjected the material to 5-h reduction treatments in hydrogen at 500, 600, and 700 °C, followed by XRD testing and SEM morphology characterization (Figure S26, Supporting Information). The results indicate that exsolution phenomena are not prominent at 500 °C. However, as the temperature increases to 600 and 700 °C, the exsolution phenomena become progressively more pronounced, with a trend of increasing particle size. To evaluate the reversibility of the exsolution process in BCFZY, we reduced the material in hydrogen at 600 °C for 10 h (yielding reduced-BCFZY), which was followed by re-oxidation in the air at 600 °C for 5 h (producing oxidized-BCFZY). XRD analysis indicates the Co-Fe NPs in reduced-BCFZY subsequently redissolved upon oxidation (Figure 2c; Figure S20, Supporting Information).^[39] X-ray photoelectron spectroscopy (XPS, Figure S21, Supporting Information) analysis confirmed that the Co and Fe valence states in reduced-BCFZY were lower than in BCFZY. Notably, metallic Co^0 and Fe^0 peaks were only detected in reduced-BCFZY. STEM imaging and EDS mapping confirmed the presence of Co-Fe alloy NPs in reduced-BCFZY (Figure 2d), which subsequently dissolved back into the bulk perovskite lattice upon oxidation (Figure 2e). This reversible exsolution/dissolution process is further supported by calculated dissolution energies (Figure S31, Supporting Information), as well as XRD, SEM, XPS, and ICP-OES characterizations (Figure S32 and Table S3, Supporting Information).

X-ray absorption spectroscopy was utilized to investigate the electronic and structural changes in BCFZY upon reduction and re-oxidation. Figure 2f presents the normalized Co K-edge X-ray absorption near-edge structure (XANES) spectra of all samples. Notably, the absorption edge of reduced-BCFZY had a lower energy (7721.3 eV) than that of pristine BCFZY (7722.7 eV), indicating a diminished Co valence in reduced-BCFZY relative to pristine one. This observation is consistent with the Co reduction results from simulation calculations and molecular orbital analysis (Figure 1) as well as the XPS results (Figure S21, Supporting Information). Crucially, upon re-oxidation, oxidized-BCFZY exhibited an increase in absorption edge energy, reverting to the pristine BCFZY value of 7722.7 eV. These data collectively provide further evidence of the material's self-recoverable capability.

The local structure, bonding, and coordination of Co were investigated using extended X-ray absorption fine structure (EXAFS) analysis. The Fourier transform of the k^3 -weighted Co K-edge EXAFS spectrum is presented in Figure 2g. The dominant peak observed at $\approx 1.4 \text{ \AA}$ corresponds to the Co–O bond, while the other peak at $\approx 2.3 \text{ \AA}$ is attributed to the Co–Co or Co–Fe bonds.^[40] In reduced-BCFZY, the estimated Co–Co and Co–Fe bond lengths are consistent with the simulated values (2.3 Å) and XRD characterization (Figure 2c; Figure S20, Supporting Information). For oxidized-BCFZY, the main peak observed $\approx 1.4 \text{ \AA}$, which aligns with the Co–O bond length in pristine BCFZY, was observed again. This observation suggests that the Co(–Fe) NPs, initially exsolved during the reduction in hy-

drogen, can redissolve into the perovskite matrix upon oxidation. The wavelet transform for EXAFS data confirms the peak transition sequence from Co–O to Co–Co or Co–Fe and back to Co–O, supporting the reversible exsolution/dissolution process (Figure 2h). A comparable trend is evident in XANES and EXAFS analysis of the Fe K-edge, with Fe valence decreasing in reduced-BCFZY and rising in oxidized-BCFZY (Figure S23, Supporting Information).

2.5. Device Performance

BCFZY stands out as a promising electrode material for symm-PCFCs due to its excellent HOR and ORR electrocatalytic activity. Its distinct advantage is a self-recovery mechanism (reversible exsolution/dissolution) that reverses performance degradation. As schematically illustrated in Figure 3a, the self-recovery process involves four redox stages: Stages 1 and 2 show Co-Fe particles exsolving to boost hydrogen adsorption and HOR efficiency. At high temperatures, any performance drop caused by particle agglomeration is reversed by their re-dissolution from Stage 2 to 3. The transition from Stage 3 to 4 and returning to Stage 1 demonstrates BCFZY's ability to self-recover, ensuring sustained performance in symm-PCFCs.

To assess the performance of symm-PCFC, a button cell with a BZCYb electrolyte (100 μm thick) and BCFZY electrodes (20 μm thick) on both sides was assembled (Figure S24, Supporting Information). During operation, pure hydrogen was supplied as fuel to the anode side, while the cathode side was exposed to 3% H_2O air. As shown in Figure 3b, the symm-PCFC reached peak power densities of 350, 233, and 131 mW cm^{-2} at 600, 550, and 500 °C, respectively, which exceed many previously reported symm-PCFCs and symmetric SOFCs (Table S2, Supporting Information). A stability test was conducted at 600 °C with a constant current of 0.45 A cm^{-2} , as shown in Figure 3c. Notably, significant degradation in performance was observed after ≈ 60 h. Thus, we implemented a recovery operation to replace anode/cathode atmosphere switching. This recovery operation consisted of a 30 min N_2 purge, followed by a 60 min re-oxidation using a 50% O_2 -50% N_2 mixture, and concluded with another 30 min N_2 purge. Remarkably, after enforcing these conditions, the symm-PCFC recovered its initial performance and remained stable until the 80 h mark. This self-recovery capability also equips the cell to resolve performance degradation issues caused by occasional gas leaks or shutdowns during actual operation.

Ten further self-recovery cycles verified the stability of the prepared symm-PCFC, with the peak power density remaining stable after each cycle (Figure 3d). The BCFZY/BZCYb interface remained robust, showing no signs of delamination or detachment after these repeated self-recovery cycles (Figure S33, Supporting Information). The BCFZY-based cell also exhibited versatility in using carbon-based fuels without significant and identifiable coking deposition (Figure S25, Supporting Information). Operating on methanol, the cell achieved peak power densities of 287, 193, and 103 mW cm^{-2} at 600, 550, and 550 °C, respectively. With methane, the peak power densities were 221, 126, and 64 mW cm^{-2} at 600, 550, and 550 °C, respectively.

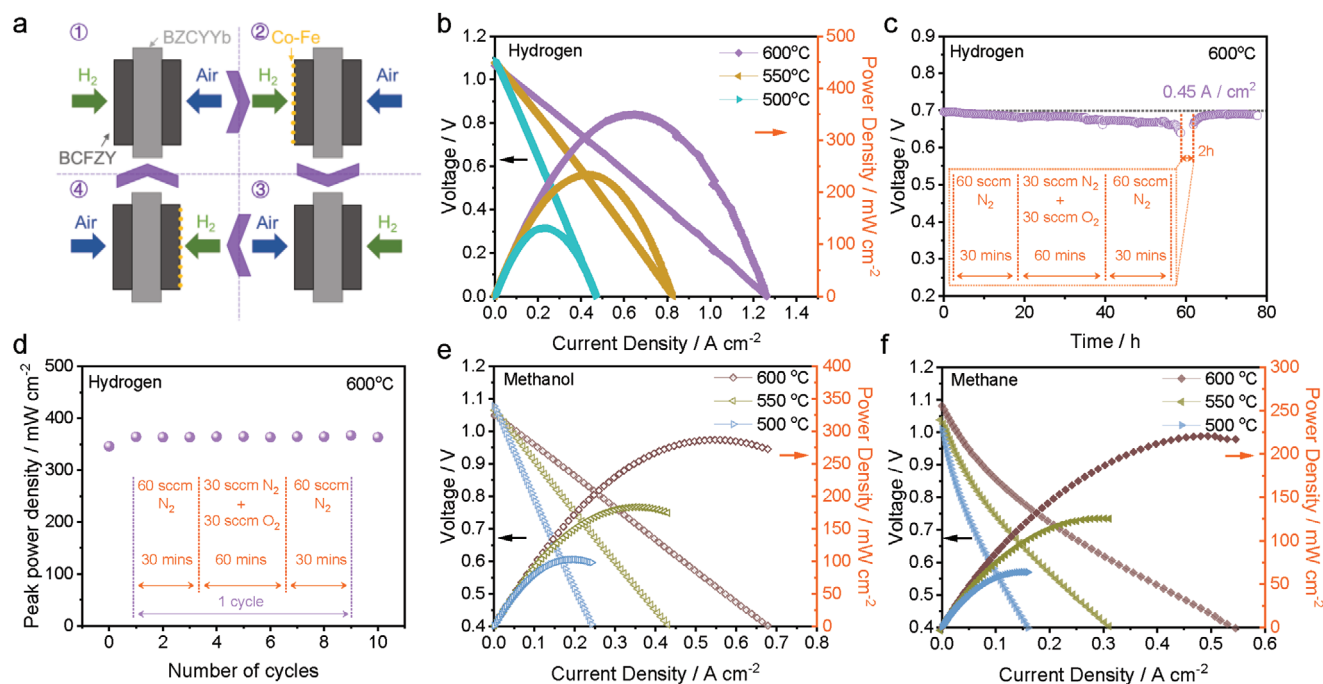


Figure 3. Electrochemical performance and durability of symm-PCFC. a) Schematic illustration of the redox operation of a self-recovering symm-PCFC with BCFZY|BZCYYb|BCFZY configuration. b) *I*-*V* and *I*-*P* curves of the symm-PCFC in hydrogen fuel at 500–600 °C. c) Operational stability of the symm-PCFC in hydrogen fuel at 600 °C. A recovery operation cycle consists of a 30 min nitrogen purge, a 60 min re-oxidation, and another 30 min nitrogen purge. d) Peak power density after several recovery operation cycles, each performance test was performed after 2 h of hydrogen reduction following the completion of the recovery operation cycle. The *I*-*V* and *I*-*P* curves of the symm-PCFC at 500–600 °C in e) methanol fuel, and f) methane fuel.

3. Conclusion

This work introduces a novel self-recoverable symm-PCFC design employing BCFZY as the bi-functional electrode. DFT calculations and molecular orbital theory analysis reveal that TM–O bond strength plays a pivotal role in determining BCFZY's bi-functionality as this material can trigger the reversible exsolution and dissolution of NPs. Experimental observations, including XRD, STEM-EDS, and XAS characterizations, confirm the computational insights, demonstrating the reversible exsolution and re-dissolution of Co-Fe NPs from and to the BCFZY matrix upon reduction and oxidation, respectively. Notably, the integration of these exsolved NPs within BCFZY enhances fuel dissociation, thereby reducing ASR in hydrogen-containing atmospheres. The symm-PCFC, fabricated and tested with hydrogen, methanol, and methane as fuels, exhibited peak power densities of 350, 287, and 221 mW cm⁻² at 600 °C, respectively. Most importantly, the reversible exsolution and dissolution of NPs, employed to avert structural damage, substantially enhance the high-performance operational longevity of the fuel cell. This method emerges as a promising material design approach, aimed at developing symm-PCFCs that exhibit both high performance and stability.

Supporting Information

Supporting Information is available from the Wiley Online Library or from the author.

Acknowledgements

The authors gratefully acknowledge the financial support given by the Research Grant Council of Hong Kong (16201820 and 16201622) and the National Natural Science Foundation of China (22309113). The authors are grateful to the Materials Characterization and Preparation Facility (MCPF) of the Hong Kong University of Science and Technology for their assistance in experimental characterizations. The authors would like to thank HKUST Fok Ying Tung Research Institute and National Supercomputing Center in Guangzhou Nansha sub-center for providing high-performance computational resources. M.R. gratefully acknowledges the support from the Research Grants Council of Hong Kong through the Hong Kong Ph.D. Fellowship Scheme (HKPFS). F.C. thanks the University of Bayreuth and the Bavarian Center for Battery Technology (BayBatt) for providing start-up funds. Upon editing the manuscript, the authors used Gemini Advanced to improve readability. After using this tool, the authors reviewed and re-edited the content as needed. Dr. M. Ellwood, the communication tutor of the Department of Mechanical and Aerospace Engineering, HKUST, provided additional help in editing the writing. The authors take full responsibility for the content of the published article.

Conflict of Interest

The authors declare no conflict of interest.

Author Contributions

Y.W., Z.W., and K.Y. contributed equally to this work. Y.W. and F.C. conceived and designed the project. Y.W. and K.Y. performed the materials synthesis, performance measurements, and basic characterizations. Y.W.,

Z.W., and J.L. performed the ab initio simulations. Z.H. performed the XAS characterization. Y.S., J.L., Z.Z., Y.T., S.X., Y.L., H.M.L., F.L., Q.C., and Z.Y. analyzed and discussed the data. Y.W., Z.W., M.J.R., and F.C. drafted the manuscript. All authors revised and reviewed the manuscript.

Data Availability Statement

The data that support the findings of this study are available from the corresponding author upon reasonable request.

Keywords

exsolution/dissolution, protonic ceramic fuel cells, self-recoverable, symmetric

Received: March 20, 2024

Revised: June 21, 2024

Published online: August 1, 2024

- [1] a) Y. Song, Y. Chen, W. Wang, C. Zhou, Y. Zhong, G. Yang, W. Zhou, M. Liu, Z. Shao, *Joule* **2019**, 3, 2842; b) C. Duan, J. Tong, M. Shang, S. Nikodemski, M. Sanders, S. Ricote, A. Almansoori, R. O'Hayre, *Science* **2015**, 349, 1321.
- [2] a) Y. Song, J. Liu, Y. Wang, D. Guan, A. Seong, M. Liang, M. J. Robson, X. Xiong, Z. Zhang, G. Kim, Z. Shao, F. Ciucci, *Adv. Energy Mater.* **2021**, 11, 2101899; b) S. H. Hwang, S. K. Kim, J.-T. Nam, J.-S. Park, *Int. J. Hydrogen Energy* **2021**, 46, 1076; c) K. Huang, S. C. Singhal, *J. Power Sources* **2013**, 237, 84; d) Y. Wang, Y. Song, J. Liu, K. Yang, X. Lin, Z. Yang, F. Ciucci, *Adv. Energy Sustainability Res.* **2022**, 3, 2100171; e) Z. Han, Y. Wang, Z. Yang, M. Han, *J. Mater. Sci. Technol.* **2016**, 32, 681.
- [3] Y. Tian, N. Abhishek, C. Yang, R. Yang, S. Choi, B. Chi, J. Pu, Y. Ling, J. T. S. Irvine, G. Kim, *Matter* **2022**, 5, 482.
- [4] J. Zamudio-García, L. Caizán-Juanarena, J. M. Porras-Vázquez, E. R. Losilla, D. Marrero-López, *J. Power Sources* **2022**, 520, 230852.
- [5] D. Wachsman Eric, T. Lee Kang, *Science* **2011**, 334, 935.
- [6] a) M. Papac, V. Stevanović, A. Zakutayev, R. O'Hayre, *Nat. Mater.* **2021**, 20, 301; b) L. Yang, S. Wang, K. Blinn, M. Liu, Z. Liu, Z. Cheng, M. Liu, *Science* **2009**, 326, 126; c) Z. Wang, Y. Wang, J. Wang, Y. Song, M. J. Robson, A. Seong, M. Yang, Z. Zhang, A. Belotti, J. Liu, G. Kim, J. Lim, Z. Shao, F. Ciucci, *Nat. Catal.* **2022**, 5, 777; d) J. Liu, J. K. Kim, Y. Wang, H. Kim, A. Belotti, B. Koo, Z. Wang, W. Jung, F. Ciucci, *Energy Environ. Sci.* **2022**, 15, 4069.
- [7] a) J. Kim, S. Sengodan, S. Kim, O. Kwon, Y. Bu, G. Kim, *Renew. Sust. Energ. Rev.* **2019**, 109, 606; b) J. C. Ruiz-Morales, D. Marrero-López, J. Canales-Vázquez, J. T. S. Irvine, *RSC Adv.* **2011**, 1, 1403; c) C. Yang, Z. Yang, C. Jin, G. Xiao, F. Chen, M. Han, *Adv. Mater.* **2012**, 24, 1439.
- [8] X. Xu, W. Wang, W. Zhou, Z. Shao, *Small Methods* **2018**, 2, 1800071.
- [9] Z. Han, Y. Wang, Y. Yang, L. Li, Z. Yang, M. Han, *J. Alloys Compd.* **2017**, 703, 258.
- [10] D. Ding, X. Li, S. Y. Lai, K. Gerdes, M. Liu, *Energy Environ. Sci.* **2014**, 7, 552.
- [11] D. Neagu, J. T. S. Irvine, J. Wang, B. Yildiz, A. K. Opitz, J. Fleig, Y. Wang, J. Liu, L. Shen, F. Ciucci, B. A. Rosen, Y. Xiao, K. Xie, G. Yang, Z. Shao, Y. Zhang, J. Reinke, T. A. Schmauss, S. A. Barnett, R. Maring, V. Kyriakou, U. Mushtaq, M. N. Tsampas, Y. Kim, R. O'Hayre, A. J. Carrillo, T. Ruh, L. Lindenthal, F. Schrenk, C. Rameshan, et al., *J. Phys. Energy* **2023**, 5, 031501.
- [12] K. Kim, B. Koo, Y.-R. Jo, S. Lee, J. K. Kim, B.-J. Kim, W. Jung, J. W. Han, *Energy Environ. Sci.* **2020**, 13, 3404.
- [13] H. Kim, C. Lim, O. Kwon, J. Oh, M. T. Curran, H. Y. Jeong, S. Choi, J. W. Han, G. Kim, *Nat. Commun.* **2021**, 12, 6814.
- [14] P. B. Managutti, S. Tymen, X. Liu, O. Hernandez, C. Prestipino, A. Le Gal La Salle, S. Paul, L. Jalowiecki-Duhamel, V. Dorcet, A. Billard, P. Briois, M. Bahout, *ACS Appl. Mater. Interfaces* **2021**, 13, 35719.
- [15] L. Zhang, W. Sun, C. Xu, R. Ren, X. Yang, J. Qiao, Z. Wang, K. Sun, *J. Mater. Chem. A* **2020**, 8, 14091.
- [16] C. Duan, R. Kee, H. Zhu, N. Sullivan, L. Zhu, L. Bian, D. Jennings, R. O'Hayre, *Nat. Energy* **2019**, 4, 230.
- [17] J. Song, C. Wei, Z.-F. Huang, C. Liu, L. Zeng, X. Wang, Z. J. Xu, *Chem. Soc. Rev.* **2020**, 49, 2196.
- [18] M. Liang, Y. Wang, Y. Song, D. Guan, J. Wu, P. Chen, A. Maradesa, M. Xu, G. Yang, W. Zhou, W. Wang, R. Ran, F. Ciucci, Z. Shao, *Appl. Catal. B: Environ.* **2023**, 331, 122682.
- [19] a) C. Duan, D. Hook, Y. Chen, J. Tong, R. O'Hayre, *Energy Environ. Sci.* **2017**, 10, 176; b) Q. Wang, S. Ricote, M. Chen, *Electrochim. Acta* **2023**, 446, 142101.
- [20] a) J. H. Kim, J. K. Kim, J. Liu, A. Curcio, J.-S. Jang, I.-D. Kim, F. Ciucci, W. Jung, *ACS Nano* **2021**, 15, 81; b) J. Wang, D. Kalaev, J. Yang, I. Waluyo, A. Hunt, J. T. Sadowski, H. L. Tuller, B. Yildiz, *J. Am. Chem. Soc.* **2023**, 145, 1714.
- [21] Y. Yang, J. Li, Y. Sun, *Chem. Eng. J.* **2022**, 440, 135868.
- [22] C. A. Ballhausen, H. B. Gray, *Molecular Orbital Theory: An Introductory Lecture Note and Reprint Volume*, WA Benjamin, Inc., Los Angeles, CA, **1965**, 102.
- [23] S. L. Millican, A. M. Deml, M. Papac, A. Zakutayev, R. O'Hayre, A. M. Holder, C. B. Musgrave, V. Stevanović, *Chem. Mater.* **2022**, 34, 510.
- [24] C. Chen, Z. M. Baiyee, F. Ciucci, *Phys. Chem. Chem. Phys.* **2015**, 17, 24011.
- [25] D. Zavickis, G. Zvejnieks, A. Chesnokov, D. Gryaznov, *Solid State Ionics* **2022**, 375, 115835.
- [26] E. A. Kotomin, Y. A. Mastrikov, M. M. Kuklja, R. Merkle, A. Roytburd, J. Maier, *Solid State Ionics* **2011**, 188, 1.
- [27] a) X. Wang, W. Li, C. Zhou, M. Xu, Z. Hu, C.-W. Pao, W. Zhou, Z. Shao, *ACS Appl. Mater. Interfaces* **2023**, 15, 1339; b) Y. Xu, F. Hu, Y. Guo, J. Zhang, Y. Huang, W. Zhou, J. Sun, B. He, L. Zhao, *Sep. Purif. Technol.* **2022**, 297, 121482.
- [28] A. Kulkarni, S. Siahrostami, A. Patel, J. K. Nørskov, *Chem. Rev.* **2018**, 118, 2302.
- [29] J. Cao, Y. Ji, Z. Shao, *Energy Environ. Sci.* **2022**, 15, 2200.
- [30] M. Probert, *Contemporary Physics* **2011**, 52, 77.
- [31] K. A. Moltved, K. P. Kepp, *J. Phys. Chem. C* **2019**, 123, 18432.
- [32] A. M. Deml, V. Stevanović, C. L. Muhich, C. B. Musgrave, R. O'Hayre, *Energy Environ. Sci.* **2014**, 7, 1996.
- [33] M. F. Hoedl, C. Ertural, R. Merkle, R. Dronskowski, J. Maier, *J. Phys. Chem. C* **2022**, 126, 12809.
- [34] a) O. Kwon, S. Sengodan, K. Kim, G. Kim, H. Y. Jeong, J. Shin, Y.-W. Ju, J. W. Han, G. Kim, *Nat. Commun.* **2017**, 8, 15967; b) M. R. Bin Mamtaz, Z. Wang, A. Belotti, E. Quattrocchi, J. Yu, J. Liu, F. Ciucci, *Energy Fuels* **2021**, 35, 15084.
- [35] Y. Yang, Y. Wang, Z. Yang, Z. Lei, C. Jin, Y. Liu, Y. Wang, S. Peng, *J. Power Sources* **2019**, 438, 226989.
- [36] J. K. Nørskov, T. Bligaard, A. Logadottir, J. R. Kitchin, J. G. Chen, S. Pandalov, U. Stimming, *J. Electrochem. Soc.* **2005**, 152, J23.
- [37] J. Kim, Y. J. Kim, M. Ferree, S. Gunduz, A. C. Co, M. Kim, U. S. Ozkan, *Appl. Catal. B: Environ.* **2023**, 321, 122026.
- [38] T. Zhang, Y. Zhao, X. Zhang, H. Zhang, N. Yu, T. Liu, Y. Wang, *ACS Sustainable Chem. Eng.* **2019**, 7, 17834.
- [39] T. Zhu, H. E. Troiani, L. V. Mogni, M. Han, S. A. Barnett, *Joule* **2018**, 2, 478.
- [40] H. Zhang, W. Zhou, T. Chen, B. Y. Guan, Z. Li, X. W. Lou, *Energy Environ. Sci.* **2018**, 11, 1980.